

## RANS-VOF Solver for Solitary Wave Run-up on A Circular Cylinder<sup>\*</sup>

CAO Hong-jian (曹洪建) and WAN De-cheng (万德成)<sup>1</sup>

*State Key Laboratory of Ocean Engineering, School of Naval Architecture, Ocean and Civil Engineering,  
Shanghai Jiao Tong University, Collaborative Innovation Center of Advanced Ship and Deep-Sea  
Exploration, Shanghai 200240, China*

(Received 20 April 2013; received revised form 18 March 2014; accepted 30 June 2014)

### ABSTRACT

Simulation of solitary wave run-up on a vertical circular cylinder is carried out in a viscous numerical wave tank developed based on the open source codes OpenFOAM. An incompressible two-phase flow solver naoe-FOAM-SJTU is used to solve the Reynolds-Averaged Navier–Stokes (RANS) equations with the SST  $k-\omega$  turbulence model. The PISO algorithm is utilized for the pressure-velocity coupling. The air-water interface is captured via Volume of Fluid (VOF) technique. The present numerical model is validated by simulating the solitary wave run-up and reflected against a vertical wall, and solitary wave run-up on a vertical circular cylinder. Comparisons between numerical results and available experimental data show satisfactory agreement. Furthermore, simulations are carried out to study the solitary wave run-up on the cylinder with different incident wave height  $H$  and different cylinder radius  $a$ . The relationships of the wave run-up height with the incident wave height  $H$ , cylinder radius  $a$  are analyzed. The evolutions of the scattering free surface and vortex shedding are also presented to give a better understanding of the process of nonlinear wave–cylinder interaction.

**Key words:** RANS; VOF; solitary wave; circular cylinder; numerical wave tank; naoe-FOAM-SJTU solver

### 1. Introduction

Wave run-up on structures is a highly nonlinear phenomenon, which can cause unexpected damage to offshore structures. The design of offshore structures requires accurate prediction of the maximum wave run-up height to maintain sufficient airgap below the platform deck. Therefore, the investigation of wave run-up becomes more and more significant with the increasing number of offshore platforms and wind farms built for human activities.

Cylindrical piles have been widely used as the foundation of coastal and offshore structures. In the case of hazardous sea conditions such as hurricanes, storms and tsunamis caused by undersea earthquake, the piles may suffer great impact loads, and the large wave run-up on the vertical piles may cause great pressure loads on the deck, even cause green water problem. Thus, the study of the nonlinear water wave run-up on cylindrical piles has great significance for the design of maritime structures.

The nonlinear theory for wave diffraction by obstacles in shallow water has been studied for several decades. Owing to the full nonlinear characteristics, solitary wave is often used to study the nonlinear

---

<sup>\*</sup> This work was financially supported by the National Natural Science Foundation of China (Grant Nos. 51379125, 51411130131, and 11432009), Program for Professor of Special Appointment (Eastern Scholar) at Shanghai Institutions of Higher Learning (Grant No. 2013022), and the National Basic Research Program of China (973 Program, Grant No. 2013CB036103).

<sup>1</sup> Corresponding author. E-mail: dcwan@sjtu.edu.cn

wave diffraction by structures. In previous studies, the focus is mainly concentrated on the solitary wave force on structures. Isaacson (1983) applied the boundary integral equation method to the problem of a solitary wave propagating past a vertical circular cylinder, and calculated the force on the cylinder by an integral equation based on Green's theorem. Chen *et al.* (1989) proposed a semi-analytic spectral method for solving the same problem. Wang *et al.* (1992) investigated a three-dimensional scattering of solitary waves by a vertical cylinder in shallow water numerically based on the generalized Boussinesq two-equation model, in which both the wave force on the cylinder and the evolution of the scattering wave field were numerically evaluated. Yates and Wang (1994) reported an experimental study of solitary waves scattered by a vertical cylinder. Experimental data were presented for the wave elevations and the forces on the vertical circular cylinder. Basmat and Ziegler (1998) employed the second-order Boussinesq equations for diffraction of the solitary wave by a vertical cylinder, which gave more accurate results of force. Ohya (1990) studied the solitary wave force acting on a large vertical cylinder by using a time-stepping method to improve the conventional boundary element method.

In recent years, numerous numerical methods have been applied to the nonlinear wave diffraction problems. Mo *et al.* (2007) proposed a three-dimensional model for calculating the non-breaking wave force on vertical piles. The numerical model is based on solving the Euler equations with Finite Volume Method (FVM) and capturing the free surface by Volume of Fluid (VOF) approach. Zhao *et al.* (2007) carried out numerical simulations of solitary wave scattering by a circular cylinder group. The Finite Element Method (FEM) was used to discretize the generalized Boussinesq equations. Zhong and Wang (2008) proposed a time-accurate stabilized finite-element model to investigate nonlinear wave diffraction problems, and the problem of solitary wave–cylinder interaction was studied as a test case. Ning *et al.* (2008) modeled the nonlinear wave interaction with maritime structures by solving the Boussinesq-type equations on a Cartesian cut-cell grid. Most of above methods were based on either the potential flow theory or neglecting the fluid viscous effect. With the improvement of computing capability and parallel computation technique, the Reynolds-Averaged Navier–Stokes (RANS) model becomes more and more popular for solving hydrodynamic problem in offshore and ocean engineering. Therefore more details of the flow field near structures are required, especially the fluid viscous effects.

This paper presents the numerical investigation of solitary wave run-up on a vertical surface-piercing circular cylinder in the viscous numerical wave tank (NWT). The fluid viscous effect is taken into account in the simulations. The results of wave run-up and wave impact forces on the cylinder are compared with the available experimental data. The details of the flow field including velocity, pressure, and the vortex shedding from the cylinder are presented and analyzed, which can improve the understanding of the characteristics of solitary wave interaction with vertical cylinder.

## 2. Numerical Methods

The present simulations are carried out with a CFD solver called naoe-FOAM-SJTU (Shen *et al.*, 2012), which is an incompressible viscous two-phase flow solver developed specially for solving the hydrodynamic problems involved in offshore and ocean engineering. This solver is programmed within the framework of OpenFOAM-2.0.1, with RANS equations as the governing equations and VOF

method for treating the free surface. In addition, numerical wave generator and wave damping zone are added to construct a complete NWT module, with which various types of waves can be generated, such as regular wave, irregular wave, and solitary wave (Zha and Wan, 2011; Cao *et al.*, 2011a, 2011b; Cao and Wan, 2012). This solver also includes 6-degree-of-freedom (6-DOF) body motion module and mooring system module for simulating the motion of floating body with or without mooring lines.

## 2.1 Governing Equations

Assumed that both the water and air are incompressible viscous Newtonian fluid, the RANS equations are employed as the governing equations, which can be expressed as follows:

$$\frac{\partial(\rho U_i)}{\partial x_i} = 0; \quad (1)$$

$$\frac{\partial U_i}{\partial t} + \frac{\partial(U_i U_j)}{\partial x_j} = -\frac{1}{\rho} \frac{\partial P}{\partial x_i} + \frac{\partial}{\partial x_j} \left[ \frac{\mu_{\text{eff}}}{\rho} \left( \frac{\partial U_i}{\partial x_j} + \frac{\partial U_j}{\partial x_i} \right) \right] + g_i - \frac{\partial(\overline{u'_i u'_j})}{\partial x_j}, \quad (2)$$

where  $U_i$  denotes the fluid velocity component in the  $i$ -th direction;  $P$  is the pressure;  $\rho$  is the fluid density;  $g_i$  denotes the acceleration of gravity;  $u'$  denotes the fluctuating velocity component;  $\mu_{\text{eff}} = \mu + \mu_t$ ,  $\mu$  is the molecular viscosity, and  $\mu_t$  is the turbulent eddy viscosity.

## 2.2 SST $k - \omega$ Turbulence Model

The Menter's Shear Stress Transport (SST)  $k - \omega$  turbulence model is employed (Menter, 1994), and the turbulent kinetic energy  $k$  and the specific dissipation rate  $\omega$  are governed by:

$$\frac{\partial(\rho k)}{\partial t} + \frac{\partial(\rho U_j k)}{\partial x_j} = P_k - \beta^* \rho \omega k + \frac{\partial}{\partial x_j} \left[ (\mu + \sigma_k \mu_t) \frac{\partial k}{\partial x_j} \right]; \quad (3)$$

$$\frac{\partial(\rho \omega)}{\partial t} + \frac{\partial(\rho U_j \omega)}{\partial x_j} = \frac{\gamma}{\nu_t} P_k - \beta \rho \omega^2 + \frac{\partial}{\partial x_j} \left[ (\mu + \sigma_k \mu_t) \frac{\partial \omega}{\partial x_j} \right] + 2(1 - F_1) \frac{\rho \sigma_{\omega 2}}{\omega} \frac{\partial k}{\partial x_j} \frac{\partial \omega}{\partial x_j}, \quad (4)$$

where  $F_1$  is a harmonic function expressed as the following formula.

$$F_1 = \tanh \left\{ \min \left[ \max \left( \frac{\sqrt{k}}{\beta^* \omega d}, \frac{500\nu}{d^2 \omega} \right), \frac{4\rho\sigma_{\omega 2} k}{CD_{k\omega} d^2} \right] \right\}^4; \quad (5)$$

$$CD_{k\omega} = \max \left( 2\rho\sigma_{\omega 2} \frac{1}{\omega} \frac{\partial k}{\partial x_j} \frac{\partial \omega}{\partial x_j}, 10^{-10} \right) \quad (6)$$

and  $\nu_t = \mu_t / \rho$  is the turbulent kinematic viscosity,  $\mu_t$  is computed as:

$$\mu_t = \frac{\rho a_1 k}{\max(a_1 \omega, \Omega F_2)}; \quad (7)$$

$$F_2 = \tanh \left[ \max \left( 2 \frac{\sqrt{k}}{\beta^* \omega d}, \frac{500\nu}{d^2 \omega} \right) \right]^2, \quad (8)$$

where  $d$  is the distance between the field point and the nearest wall, and  $\Omega$  is the vorticity magnitude.

The constants are:  $\sigma_{k1} = 0.85034$ ,  $\sigma_{k2} = 1.0$ ,  $\sigma_{\omega1} = 0.5$ ,  $\sigma_{\omega2} = 0.85616$ ,  $\beta_1 = 0.075$ ,  $\beta_2 = 0.0828$ ,  $\beta^* = 0.09$ ,  $a_1 = 0.31$ ,  $\gamma_1 = 5/9$ , and  $\gamma_2 = 0.4403$ .

### 2.3 VOF Method

Numerous methods have been proposed and used for tracing or capturing the interface of multi-phase flow, such as marker-and-cell (MAC) method, VOF method, and level set method. VOF method is one of the most popular approaches because it has the following advantages: good mass conservation, computational efficiency, and easy implementation. Therefore, VOF method is applied in present work, and the volume fraction  $\alpha$  is defined as:

$$\alpha(x, t) = \begin{cases} \alpha = 0 & \text{air} \\ 0 < \alpha < 1 & \text{interface} \\ \alpha = 1 & \text{water} \end{cases} \quad (9)$$

The volume fraction  $\alpha$  needs to satisfy the following equation:

$$\frac{\partial \alpha}{\partial t} + \frac{\partial(\alpha U_i)}{\partial x_i} = 0. \quad (10)$$

During the solving procedure, the VOF method with bounded compression techniques is applied (Rusche, 2003). The necessary compression of the free surface is achieved by introducing an extra artificial compression term into Eq. (10) as follows:

$$\frac{\partial \alpha}{\partial t} + \frac{\partial(U_i \alpha)}{\partial x_i} - \frac{\partial[U_{ir} \alpha(1-\alpha)]}{\partial x_i} = 0, \quad (11)$$

in which, the compression term takes effect only on the interface due to the existence of  $(1-\alpha)\alpha$ .  $U_{ir}$  is the velocity field suitable to compress the interface, which can be obtained with the following equation:

$$U_{ir} = \mathbf{n} \cdot \min[C_\alpha |U_i|, \max(|U_i|)], \quad (12)$$

where  $\mathbf{n}$  is the unit normal vector on the interface;  $C_\alpha$  is the compression factor for controlling the strength of compression.

The density  $\rho$  and viscosity  $\nu$  are calculated by a weighting function of  $\alpha$ :

$$\begin{cases} \rho = \alpha \rho_w + (1-\alpha) \rho_a \\ \nu = \alpha \nu_w + (1-\alpha) \nu_a \end{cases} \quad (13)$$

where  $\rho_w$  and  $\rho_a$  denote the density of water and air, respectively;  $\nu_w$  and  $\nu_a$  denote the viscosity coefficient of water and air, respectively.

### 2.4 Initial and Boundary Conditions

A rectangular computational domain is selected as the model of NWT. The no-slip boundary condition is imposed on the solid wall, and the law of the wall function is applied to the  $k-\omega$  turbulence model. The symmetry boundary condition is applied to the side walls to weaken the wave reflection. The zero-gradient boundary condition is applied to the outlet. As the VOF method is used to

capture free surface, there is no need to set the kinematic and dynamic free surface boundary conditions.

At the initial time of simulations, both the air and the water are at rest. The hydrostatic pressure is initialized in the computational domain. The volume fraction is set as  $\alpha = 0$  for the cell occupied by air and  $\alpha = 1$  for the cell occupied by water. The incident wave profile and velocities of water particles at the inlet boundary are given according to the analytical solution of wave theory.

### 2.5 Pressure-Velocity Coupling

Pressure Implicit with Splitting of Operator (PISO) algorithm proposed by Issa (1986) is employed for the pressure-velocity coupling during the process of solving Navier–Stokes equations. This method uses one predictor step and two corrector steps to obtain accurate velocity and pressure, which can give stable results, especially for the unsteady flow problem.

### 2.6 Discretization Schemes

The RANS equations and the VOF transport equation are discretized by FVM. Implicit Euler scheme is for the temporal discretization. The second-order TVD limited linear scheme is applied to the convection terms of RANS equations, and the second-order central difference scheme is applied to the diffusion term. The van Leer scheme is applied to the transport equation of volume fraction  $\alpha$ .

## 3. Numerical Results and Discussion

In this section, simulations of solitary wave run-up on a vertical circular cylinder are presented. With a serial of varied incident wave heights and cylinder radii, the maximum wave run-up height and wave force are calculated and compared with the corresponding data from experiment and numerical simulation. The evolution of the free surface and vortex field are also presented and analyzed.

### 3.1 Verification of Numerical Method

Firstly, a classical two-dimensional case of solitary wave run-up on a vertical wall is simulated to validate the NWT module. The maximum wave run-up values are compared with both the experimental data and the analytical solutions. The incident solitary wave is generated by specifying the analytical solution at the inlet boundary. The solitary wave surface profile and the water particles velocities can also be given according to analytical expression, which can refer to Dean and Dalrymple (1991). The solitary wave profile is expressed as follows:

$$\eta = H \operatorname{sech}^2[k(x - ct)]; \quad k = \sqrt{3H/(4h^3)}, \quad (14)$$

where  $H$  is the solitary wave height,  $h$  is the depth of water,  $x$  is the position of solitary wave crest, and  $c = \sqrt{g(H + h)}$  is the propagating velocity of solitary wave.

A rectangular computational domain is chosen as the model of NWT, whose length is 20 m and width is 0.12 m. The origin of the coordinate system is at the intersection of the still water level and the left inlet boundary.  $x$  and  $z$  are the horizontal and vertical coordinates, respectively. The wave depth is  $h=1.0$  m. The computational domain is discretized with  $200 \times 48$  hexahedral cells with only one grid in  $y$ -direction. Cases with different incident solitary wave heights are performed. The wave height  $H$  varies

from 0.05 m to 0.65 m. After propagation through the whole wave tank, the solitary wave will run upward along the vertical wall at the right end, where the no-slip wall boundary condition is applied.

Several wave probes are arranged at the position  $x=6$  m, 8 m, 10 m, 12 m for measuring the free surface elevation. Fig. 1 shows the comparison of free surface elevation at  $x=6$  m between numerical result and analytical solution. A good agreement indicates the efficiency and accuracy of the present NWT for the solitary wave generation. Time histories of free surface elevation at all above probes are plotted in Fig. 2, showing that the solitary wave profile and wave height are kept stable during its propagation.

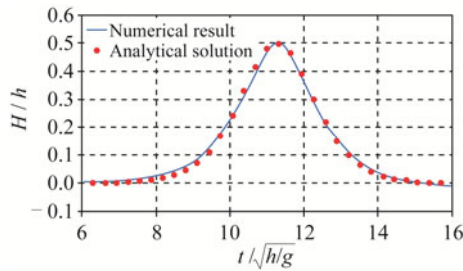


Fig. 1. Comparison of the solitary wave profile.

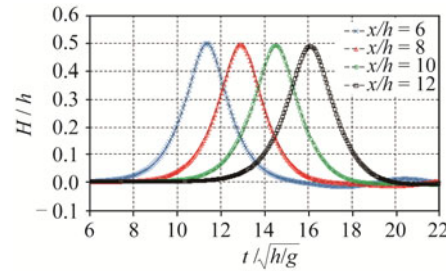


Fig. 2. Solitary wave profiles at different probes.

Fig. 3 shows the comparison of the maximum wave run-up height ( $R_{max}$ ) on the vertical wall. Experimental data come from Maxworthy (1976), while the analytical solution is obtained with the formula proposed by Byatt-Smith (1971), which is expressed as follows:

$$\frac{R_{max}}{h} = 2\frac{H}{h} + \frac{1}{2}\left(\frac{H}{h}\right)^2 + o\left(\frac{H}{h}\right)^3. \tag{15}$$

It can be seen that present numerical results agree well with the experimental data and analytical solution. However, the numerical results are a bit larger than the analytical solutions for  $H/h > 0.5$ , which may be due to the instability and strong nonlinearity of the solitary wave with large wave height.

Fig. 4 shows the instantaneous solitary wave profile along the wave tank with the wave height  $H=0.5$  m at different time.  $T_0$  represents the time when the maximum wave run-up height occurs. It is seen that the solitary wave height decreases obviously after reflected from the vertical wall, which is owing to the viscous effect and dissipation of wave energy.

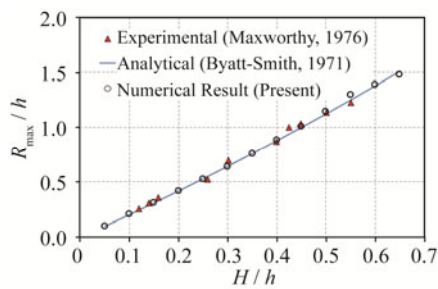


Fig. 3. Maximum run-up height on the vertical wall.

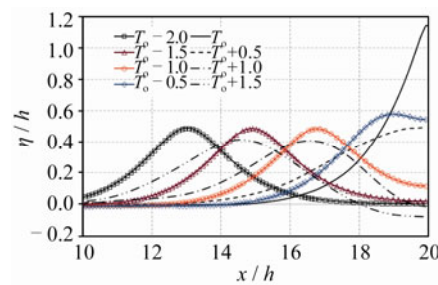
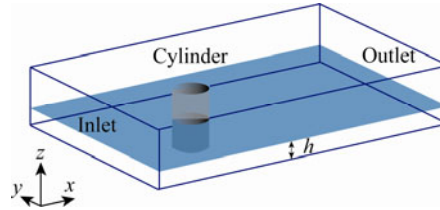


Fig. 4. Wave profile at different time for  $H/h=0.5$ .

### 3.2 Solitary Wave Interaction with A Circular Cylinder

In this section, the solitary wave interaction with a surface-piercing vertical circular cylinder is investigated. The wave force and wave run-up are calculated with considerations of different incident solitary wave heights. As the sketch of numerical model depicted in Fig. 5, the computational domain is set up with the dimensions:  $0 \text{ m} \leq x \leq 30 \text{ m}$ ,  $-10 \text{ m} \leq y \leq 10 \text{ m}$ , and  $-1.0 \text{ m} \leq z \leq 2.5 \text{ m}$ . The water depth is  $h=1.0 \text{ m}$ . A circular cylinder is fixed in the centerline of the wave tank with the distance of 10 m to the inlet boundary, whose radius is  $a=1.5875 \text{ m}$ , as same as the one used in the experiment of Yates and Wang (1994).

Fig. 5. Sketch of a solitary wave interaction with a vertical circular cylinder.



The computational mesh is shown in Fig. 6. In order to capture the free surface accurately, the finest mesh is used near the free surface along  $z$ -direction. The minimum size of the grid along  $z$ -direction is 0.01 m. The total cell number is about 0.24 million. During the simulation, the time step is adjusted with the limitation that the maximum Courant number is smaller than 0.3, and the maximum time step is smaller than 0.02 s. The initial time step is  $\Delta t=0.001 \text{ s}$ .



Fig. 6. Mesh of the computational domain.

The maximum forces on the cylinder are calculated during the simulations. The horizontal wave force are compared with the corresponding data from the work of Yates and Wang (1994) and Zhao *et al.* (2007), as shown in Fig. 7. The red dot represents the experimental data, the dash line represents the numerical results of Zhao *et al.* (2007) with FEM, and the solid line represents the present results with RANS solver. Good agreements are obtained in comparison with the experimental data, except that the present negative force is a bit larger. It is also seen that the present results are a bit better than those with FEM from Zhao *et al.* (2007), especially for the case of  $H/h=0.40$ .

In order to obtain the wave elevation and run-up height on the cylinder, several wave probes are arranged close to the cylinder surface. As shown in Fig. 8,  $\theta$  denotes the radiation angle, which is in the range  $(0^\circ, 360^\circ)$  in the counter-clockwise direction. The interval angle between two neighboring probes close to the cylinder surface is  $22.5^\circ$ . There are other four probes ( $p1, p2, p3, p4$ ) located in front of the cylinder with  $\theta=180^\circ$ , and the distance between each probe and the cylinder center are described as  $r/a=1.03, 1.66, 2.61, 4.50$ .

Fig. 9 shows the time histories of wave elevation at the probes ( $p1, p2, p3, p4$ ) for  $H/h=0.4$ . The comparisons between the present results and experimental measurement show satisfactory agreement despite some differences exist, especially for the wave elevation at the probe  $p1$ . The difference may be due to the viscous boundary layer adhered to the cylinder surface, which makes the calculated run-up value a bit larger. The comparisons indicate that the present numerical method has satisfactory efficiency and accuracy for simulating the solitary wave–cylinder interaction problem.

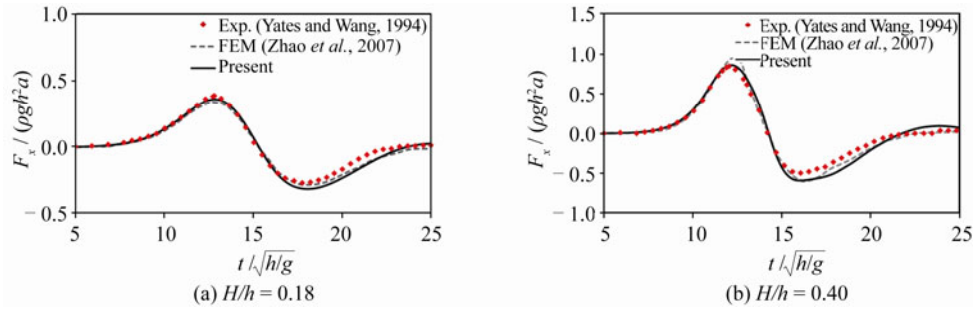


Fig. 7. Comparisons of the time histories of the horizontal wave force on the cylinder.

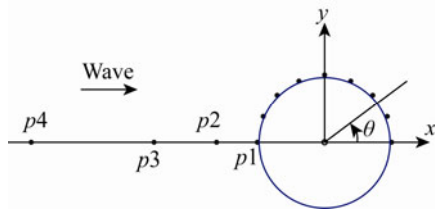


Fig. 8. Arrangement of the wave probes.

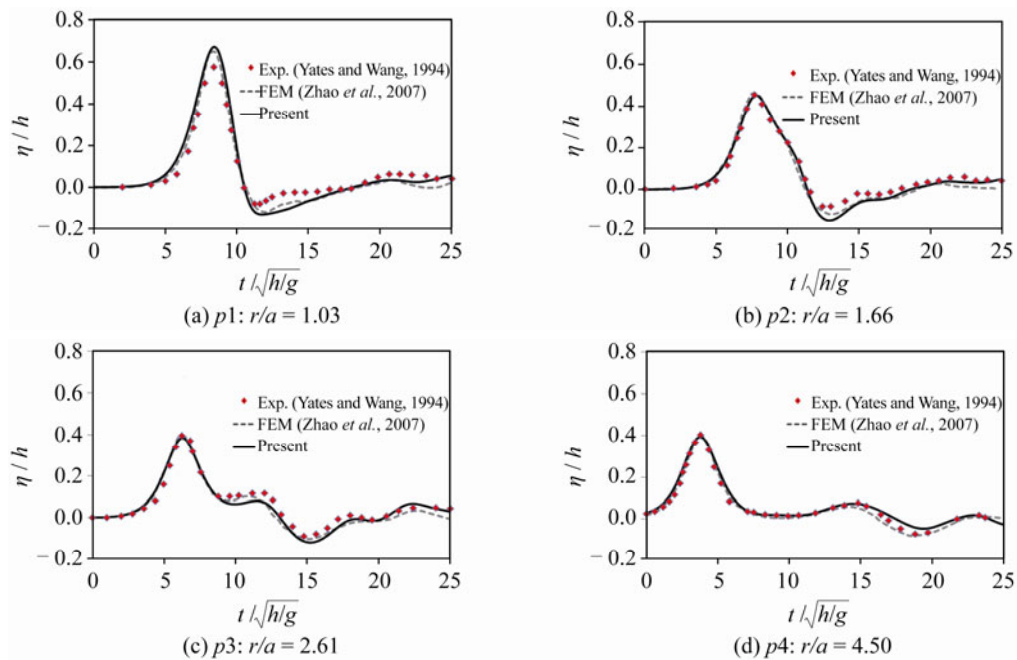
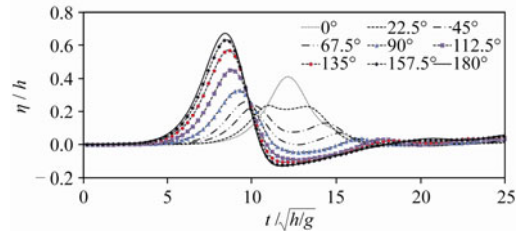


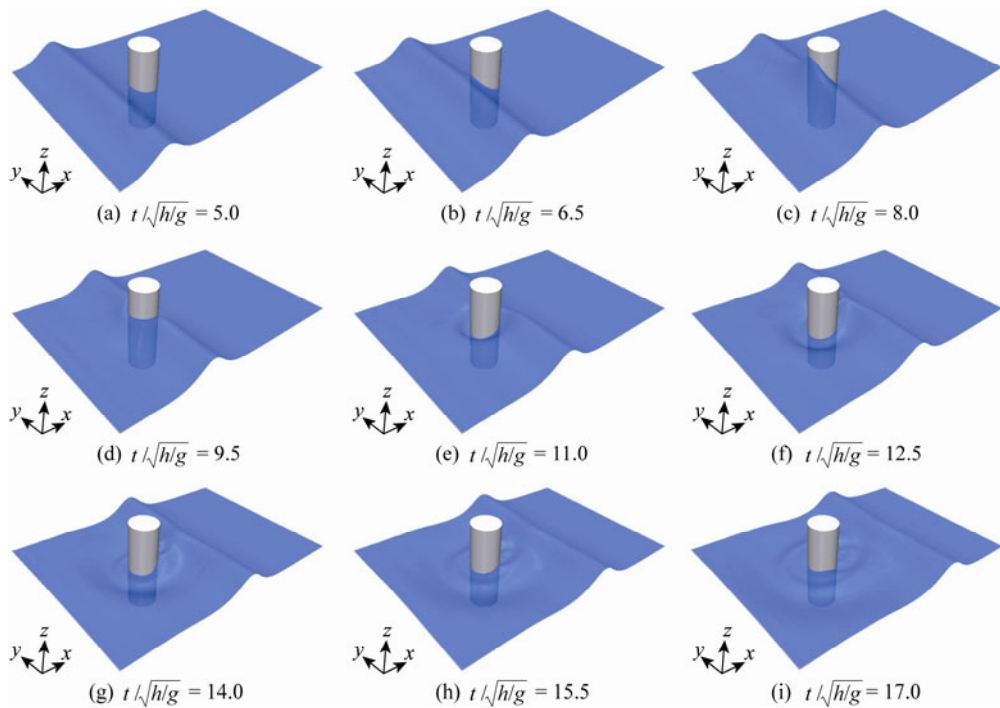
Fig. 9. Time histories of wave elevation at the probes ( $H/h=0.40$ ).

Fig. 10 shows the wave elevation at the probes close to the cylinder circle with  $\theta$  varying from  $0^\circ$  to  $180^\circ$ . Obviously, the maximum wave run-up occurs in front of the cylinder ( $\theta=180^\circ$ ). The minimum wave run-up occurs near the position with  $\theta=45^\circ$ . In addition, there is an obvious secondary peak on each curve of time history of wave elevation probed at the rare side of the cylinder such as  $\theta=22.5^\circ$ ,  $45^\circ$ , and  $67.5^\circ$ . As the probe moves to the lee point with  $\theta=0^\circ$ , the wave elevation becomes nearly the same as the incident wave height.

**Fig. 10.** Time histories of wave elevation at the probes along the cylinder surface ( $H/h=0.40$ ).



To visualize the scattering process, the free surface evolution in three-dimensional domain is shown in Fig. 11 from  $t/\sqrt{h/g} = 5$  to  $t/\sqrt{h/g} = 17$ . It is obviously seen that the wave run-up occurs at about  $t/\sqrt{h/g} = 8$ . After the solitary wave crest passing the cylinder, the free surface around the cylinder vibrates for a long time, and the wave reflected from the cylinder spreads outwards. Therefore, a wave scattering field forms around the cylinder.



**Fig. 11.** Free surface evolution of solitary wave scattering by the cylinder ( $H/h=0.4$ ).

Fig. 12 shows the scattering free surface elevation contour from  $t/\sqrt{h/g}=6.5$  to  $t/\sqrt{h/g}=14$ . The scattering free surface elevation is symmetric to the center plane of the wave tank. As the wave crest has passed the cylinder, there is a low part formed on the free surface in front of the cylinder, which moves to the opposite direction of the solitary wave propagation.

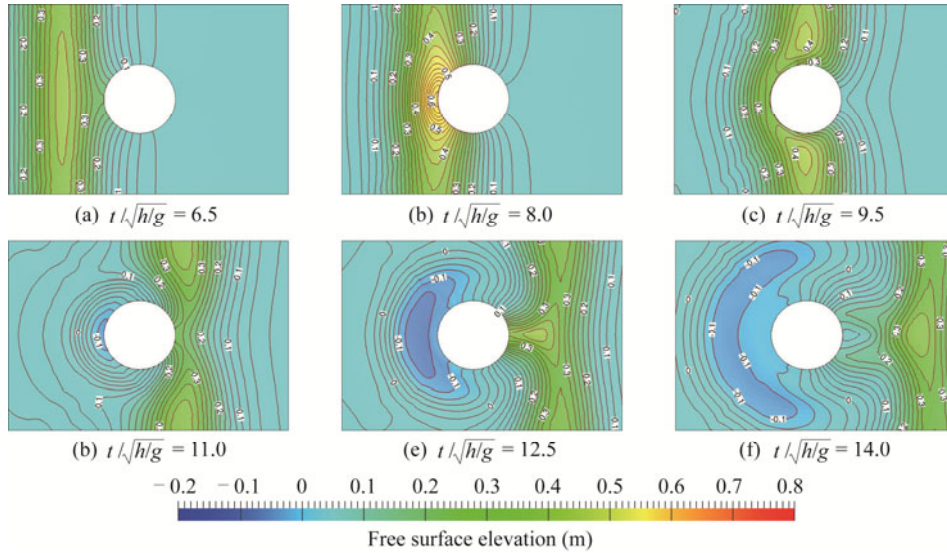


Fig. 12. Contour of free surface elevation ( $H/h=0.4$ ).

The vortex field is presented in Fig. 13 with the iso-surface  $Q=0.5$  according to  $Q$ -criterion (Hunt *et al.*, 1988). The color represents the  $x$ -component of the vorticity  $\omega_x$  that varies in the range of  $-1.0 \leq \omega_x \leq 1.0$ . As the solitary wave crest passes the cylinder, the vortex field forms due to the violent flow of free surface. The vortex is generated around the cylinder and close to the free surface, and then moves outward off the cylinder and decreases gradually.

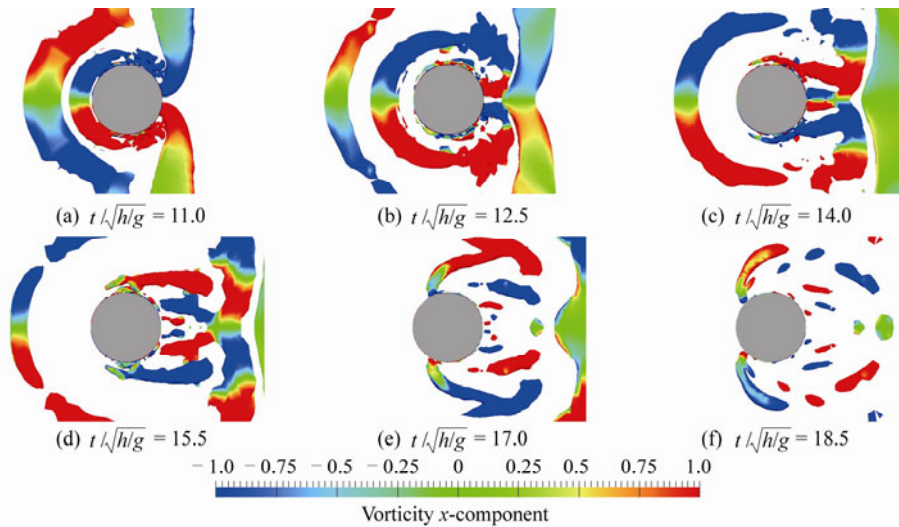


Fig. 13. Evolution of the vortex shedding ( $H/h=0.4$ ).

Fig. 14 shows the dynamic pressure contours on the cylinder surface at the instantaneous moment that the maximum wave run-up height occurs with different wave heights  $H/h=0.20, 0.40,$  and  $0.60$ . It can be seen that the maximum dynamic pressure is measured in front of the cylinder and close to the free surface. In addition, the dynamic pressure increases with the increasing wave height.

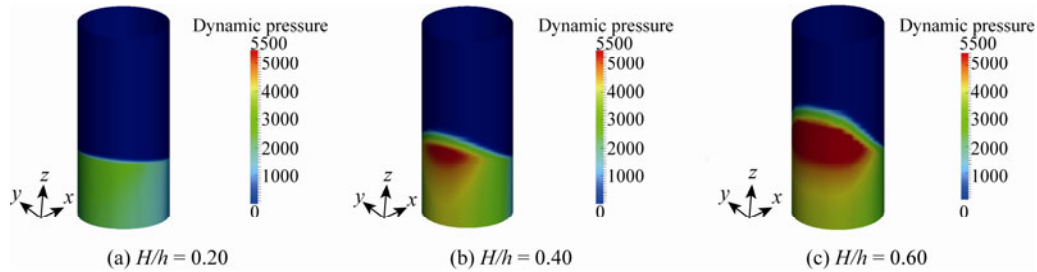


Fig. 14. Dynamic pressure contour on the cylinder surface.

Fig. 15 shows the ratio of the maximum wave run-up height to the incident wave height at the probe closest to the cylinder surface ( $r/a=1.03$ ). It is seen that the maximum run-up ratio increases with  $H/h$  almost linearly for small incident wave height ( $H/h<0.4$ ), but increases faster for larger wave height ( $H/h>0.40$ ). When  $H/h>0.6$ , the nonlinear increase of the wave run-up ratio becomes more obviously, which indicates the strongly nonlinearity existing in the wave run-up phenomenon.

Fig. 16 shows the variation of the maximum wave run-up ratio  $R_{max}/H$  along the cylinder surface for different incident wave heights. It is seen that the maximum value occurs at probes closest to the cylinder surface at the up-wave side with  $\theta=180^\circ$ , while two minimum values occur near the position with  $\theta=45^\circ$  and  $\theta=315^\circ$ , respectively. However, the positions are moving towards the lee point of the cylinder with the increasing incident wave height. The run-up ratio is about  $R_{max}/H=1.0$  at the probe close to the lee point with  $\theta=0^\circ$ .

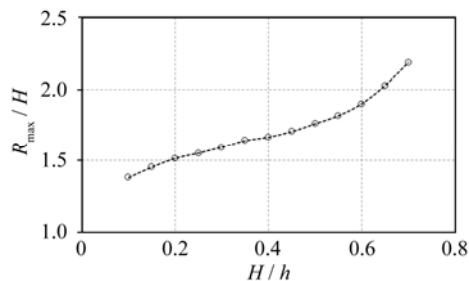


Fig. 15. Maximum wave run-up ratio for different  $H/h$ .

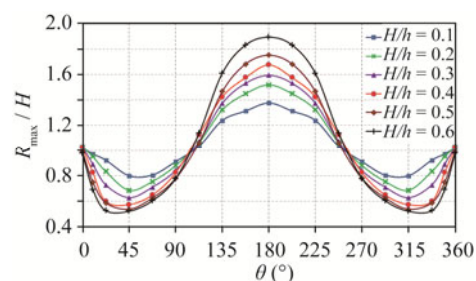


Fig. 16. Maximum wave run-up height along the cylinder.

The further studies of the solitary wave run-up and wave force on the cylinder with different radii are performed. The cylinder radius is selected as follows:  $a=0.25, 0.5, 1.0, 1.5875,$  and  $2.0$  m. The maximum horizontal wave force and wave run-up height are calculated under the same incident wave with wave height  $H=0.40$  m. Fig. 17 shows that both the horizontal force and wave run-up height increase with the increasing cylinder radius. If assuming that the cylinder radius is infinitely large, this problem can be considered as a solitary wave run-up on a vertical wall. Therefore, the upper limit of the

dimensionless wave run-up value can be obtained with Eq. (15).

Fig. 18 shows the side view of the free surface at the instantaneous moment when the maximum wave run-up occurs for different cylinder radii. It is seen that the maximum wave run-up always occurs at the upwave side of cylinder. There is a trough occurred at the rear of the cylinder for  $a = 0.5$  m. However, the trough moves to the lee point with the increasing radius. For  $a \geq 1.0$  m, there is no trough around the cylinder, and the free surface elevation around the cylinder is higher than the initial water level.

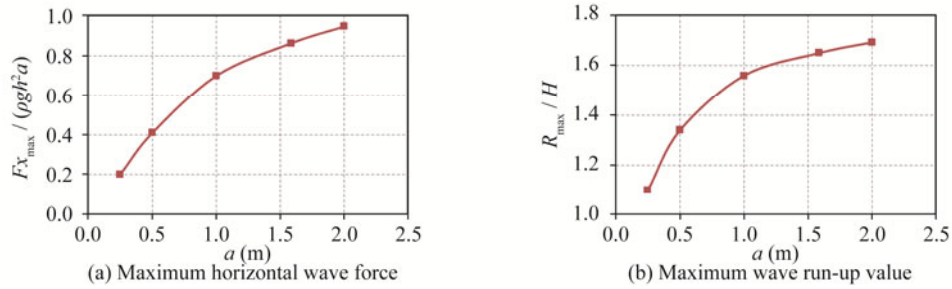


Fig. 17. Maximum horizontal wave force and wave run-up value for different cylinder radii ( $H/h=0.4$ ).

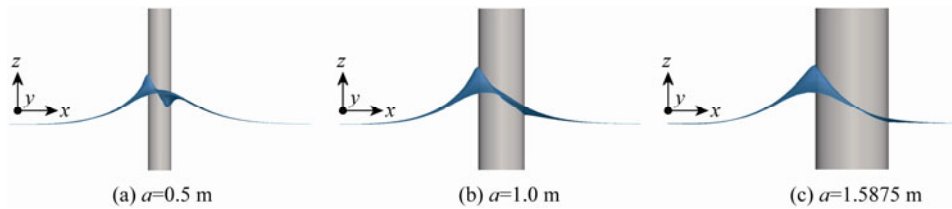


Fig. 18. Side-view of the free surface at the time when the maximum wave run-up occurs.

Fig. 19 shows the dynamic pressure contour on cylinder, which indicates that the solitary wave impact loading increases with increasing cylinder radii. The maximum pressure occurs at the upwave side of the cylinder and close to the free surface at the time when the maximum wave run-up appears.

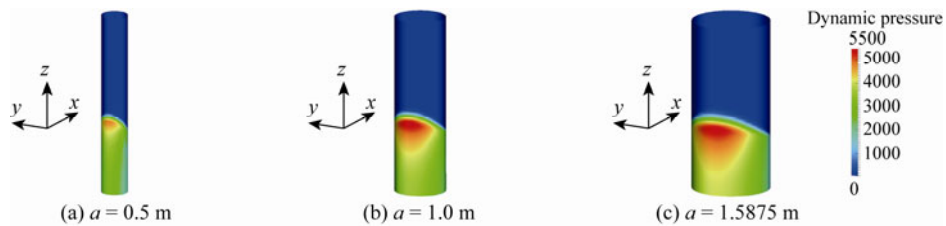


Fig. 19. Dynamic pressure contour on the cylinder surface ( $H/h=0.4$ ).

Fig. 20 shows the vortex field forms when the solitary wave crest is passing the cylinder. The vortex field is described with the iso-surface  $Q = 0.5$ . The color represents the  $x$ -component of the vorticity  $\omega_x$  that varies in the range of  $-1.0 \leq \omega_x \leq 1.0$ . With the comparison of the vortex field formed behind the cylinder with different radii  $a$ , we can see that the vortex shedding from the cylinder is

complicated in the region near the cylinder surface when the cylinder radius is small. With the increase of cylinder radius, the range of the vortex is enlarged, and the whole vortex field seems more regular and symmetric to the centerline of the wave tank. Meanwhile, the values of vorticity in the field also become larger with the increasing radius, which reflects the increasing strength of vortex shedding from the cylinder.

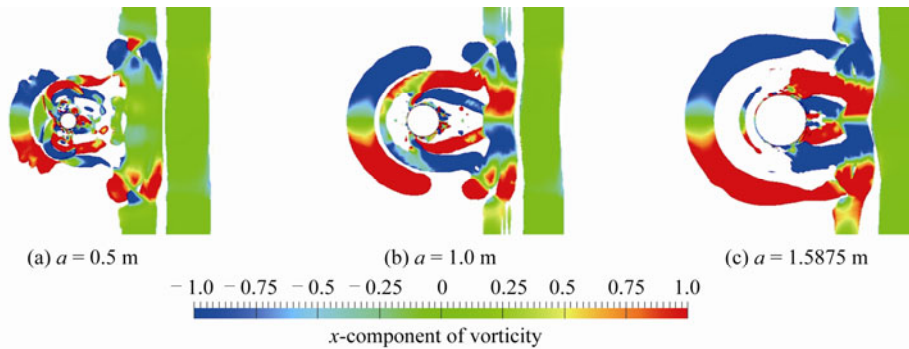


Fig. 20. Iso-surfaces of  $Q=0.5$  with different radii of cylinder ( $H/h=0.4$ ).

#### 4. Conclusions

The numerical study of solitary wave interaction with a surface-piercing vertical cylinder is performed with a new solver naoe-FOAM-SJTU. The free surface is accurately captured with the VOF method. The wave force and wave run-up on a single cylinder are calculated and compared with experimental data. Satisfactory agreement indicates the efficiency and accuracy of the present numerical methods. Furthermore, the wave run-up and wave force on the cylinder with different wave height  $H$  and different cylinder radius  $a$  are analyzed separately. It is obviously shown that both the maximum wave force and the wave run-up height increase with the increasing incident wave height and the cylinder radius  $a$ . In addition, the free surface evolution, the pressure contour on the cylinder, and the vortex shedding from the cylinder are presented to give a better understanding of the solitary wave interaction with the cylinder.

The presented numerical results indicate that the solver naoe-FOAM-SJTU is capable of solving the problem of strongly nonlinear wave-structure interaction. The predicted wave force and run-up value is reasonable and shows satisfactory agreement with corresponding data. Much more details of the flow field including pressure and vortex field can be provided for better understanding of the wave-structure problem. In the future work, the present solver will be applied to predicting the motion response of floating body in waves with its 6DOF body motion module, which will be a great help for studying the hydrodynamic performance of offshore structures.

**Acknowledgements** – The authors are most grateful to Center of HPC of Shanghai Jiao Tong University, and the Lloyd's Register Foundation (LRF) that invests in science, engineering and technology for public benefit, worldwide.

#### References

Basmat, A. and Ziegler, F., 1998. Interaction of a plane solitary wave with a rigid vertical cylinder, *Z. Angew. Math.*

- Mech.*, **78**(8): 535–543.
- Byatt-Smith, J. G. B., 1971. An integral equation for unsteady surface waves and a comment on the Boussinesq equation, *J. Fluid Mech.*, **49**(4): 625–633.
- Chen, Y. S., Chen, Y. Z. and Cao, N. Z., 1989. The diffraction of a solitary wave by a circular cylinder, *Acta Mechanica Sinica*, **5**(4): 293–300.
- Cao, H. J., Zha, J. J. and Wan, D. C., 2011a. Numerical simulation of wave run-up around a vertical cylinder, *Proc. 21st Int. Offshore Polar Eng. Conf. (ISOPE)*, Maui, Hawaii, USA, 726–733.
- Cao, H. J. and Wan, D. C., 2012. Numerical investigation of extreme wave effects on cylindrical offshore structures, *Proc. 22nd Int. Offshore Polar Eng. Conf. (ISOPE)*, Rhodes, Greece, 804–811.
- Cao, H. J., Liu, Y. C., Wan, D. C. and Yang, C., 2011b. Numerical simulation of extreme wave impact on fixed offshore platform, *Proc. 7th Int. Workshop Ship Hydrodynamics (IWSH)*, Shanghai, China, 138–143.
- Dean, R. G. and Dalrymple, R. A., 1991. *Water Wave Mechanics for Scientists and Engineers – Advanced Series on Ocean Engineering*, Vol. 2, World Scientific.
- Hunt, J. C. R., Wray, A. A. and Moin, P., 1988. Eddies, stream, and convergence zones in turbulent flows, *Stanford N.A.S.A. Center for Turbulence Research*, CTR-S88.
- Isaacson, M. D. S. Q., 1983. Solitary wave diffraction around large cylinder, *J. Waterw. Port Coast. Ocean Div.*, ASCE, **109**(1): 121–127.
- Issa, R. I., 1986. Solution of the implicitly discretised fluid flow equations by operator-splitting, *J. Comput. Phys.*, **62**(1): 40–65.
- Maxworthy, T., 1976. Experiments on collisions between solitary waves, *J. Fluid Mech.*, **76**(1): 177–186.
- Menter, F., 1994. Two-equation eddy-viscosity turbulence model for engineering applications, *AIAA J.*, **32**(8): 1598–1605.
- Mo, W., Irschik, K., Oumeraci, H. and Liu, P. L. F., 2007. A 3D numerical model for computing non-breaking wave forces on slender piles, *J. Eng. Math.*, **58**(1-4): 19–30.
- Ning, D. Z., Zang, J., Liang, Q., Taylor, P. H. and Borthwick, A. G. L., 2008. Boussinesq cut-cell model for non-linear wave interaction with coastal structures, *Int. J. Numer. Methods Fluids*, **57**(10): 1459–1483.
- Ohyama, T., 1990. A numerical method of solitary wave forces acting on a large vertical cylinder, *Proc. 22nd Conf. Coast. Eng.*, Delft, The Netherlands, **1**, 840–852.
- Rusche, H., 2003. *Computational Fluid Dynamics of Dispersed Two-phase Flows at High Phase Fractions*, London, Imperial College of Science, Technology and Medicine.
- Shen, Z. R., Cao, H. J., Ye, H. X. and Wan, D. C., 2012. *Manual of CFD Solver naoe-FOAM-SJTU*, Shanghai, Shanghai Jiao Tong University. (in Chinese)
- Wang, K. H., Wu, T. Y. and Yates, G. T., 1992. Three-dimensional scattering of solitary waves by vertical cylinder, *J. Waterw. Port Coast. Ocean Eng.*, ASCE, **118**(5): 551–566.
- Yates, G. T. and Wang, K. H., 1994. Solitary wave scattering by a vertical cylinder: experimental study, *Proc. 4th Int. Offshore Polar Eng. Conf. (ISOPE)*, Osaka, Japan, 118–124.
- Zha, J. J. and Wan, D. C., 2011. Numerical wave generation and absorption based on OpenFOAM, *The Ocean Engineering*, **29**(3): 1–12. (in Chinese)
- Zhao, M., Cheng, L., and Teng, B., 2007. Numerical simulation of solitary wave scattering by a circular cylinder array, *Ocean Eng.*, **34**(3-4): 489–499.
- Zhong, Z. and Wang, K. H., 2008. Time-accurate stabilized finite-element model for weakly nonlinear and weakly dispersive water waves, *Int. J. Numer. Methods Fluids*, **57**(6): 715–744.